SECED 2023 Conference
Earthquake Engineering & Dynamics for a Sustainable Future
14-15 September 2023, Cambridge, UK

CYCLIC AND IMPACT PROPERTIES OF RUBBERISED ALKALI-ACTIVATED CONCRETE

Mohamed ELZEADANI[1], Dan BOMPA[2] & Ahmed ELGHAZOULI[3]

Abstract: *This paper presents the rate-dependent cyclic compressive properties, and the compressive and splitting tensile impact properties of rubberised slag-based alkali-activated concrete. Crumb rubber particles of up to 60% replacement by volume of the total natural aggregates are considered. For the rate-dependent cyclic response, three different strain-rates accounting for quasi-static, moderate seismic and severe seismic conditions are investigated using a servo-hydraulic machine. The compressive and splitting tensile impact properties are performed in an instrumented drop-weight loading rig. Three impact velocities of 5, 10 and 15 m/s are considered, giving a range of strain-rates between 3 and 270 s^{-1}. The cyclic and impact mechanical properties, including the compressive strength, elastic modulus, and splitting tensile strength, reduce with higher rubber content, and are shown to be strain-rate sensitive. The unloading and reloading curves in the cyclic stress-strain response fall within the monotonic curves. Rubber addition increases the impact duration under compressive loading and alters the compressive stress-strain response under impact, resulting mainly in two main peaks and a delay in the axial crushing strain. Analytical expressions are presented to predict the unloading modulus, residual plastic strain, and unloading-reloading curves in the cyclic stress-strain response. Formulations for the dynamic increase factors of the compressive strength, elastic modulus, axial crushing strain and splitting tensile strength under a varied range of strain-rates are also provided. The results help characterise the fundamental cyclic and impact properties of rubberised alkali-activated concrete.*

Introduction

Alkali-activated concrete (AAC) avoids ordinary Portland cement (OPC) in the mix design and employs aluminosilicate precursors that are made more reactive with the help of a chemical activator (Provis, 2018). Sources of aluminosilicate precursors are myriad, but much of the available research employs well-established industrial by-products as precursors, including fly ash (FA) and ground granulated blast furnace slag (GGBS) (Provis and Bernal, 2014). Activators used need to provide sufficient alkalinity in the system to allow for the dissolution of aluminosilicate species from the precursors and form the binding gels. Such activators have traditionally been added in a soluble form (e.g., sodium hydroxide and sodium silicate solutions) (Provis and Bernal, 2014). Recent developments in AAC, however, have led to the introduction of one-part AAC, where the activator is added in a solid state to circumvent the in-situ production challenges associated with caustic soluble activators (Elzeadani et al., 2022a).

Rubberised concrete (RuC) represents another innovation in sustainable concrete materials, which involves a replacement of a proportion of the natural mineral aggregates with crumb rubber (CR) particles derived from discarded end-of-life tyres (Bompa et al., 2017). This provides a recycling path for tyres and enhances the deformation characteristics of concrete. However, this comes at the price of a reduction in mechanical properties in line with the added rubber content (Bompa et al., 2017). Researchers have capitalized on the improved deformation behaviour of RuC and investigated its response under cyclic and impact loading scenarios (Pham et al., 2020; Xu et al., 2020). The results were generally promising, indicating a significantly improved postpeak cyclic degradation behaviour and a greater sensitivity to the strain-rate with higher rubber addition.

[1] PhD Student, Imperial College London, London, United Kingdom, m.el-zeadani20@imperial.ac.uk
[2] Senior Lecturer, University of Surrey, Guildford, United Kingdom [3]
Professor, Imperial College London, London, United Kingdom

Research on the cyclic and impact properties of rubberised alkali-activated concrete (RuAAC), particularly rubberised one-part alkali-activated concrete (OP-RuAAC), has been very limited (Elzeadani et al., 2021). This study, therefore, presents an experimental evaluation of the cyclic and impact material properties of OP-RuAAC. The cyclic response is investigated under compressive loading while the impact response is investigated under compressive and splitting tensile loading. Three different volumetric crumb rubber replacement ratios of the total natural aggregates are considered, including 0, 30 and 60% replacement. The findings shed light on the effect of increasing rubber content on the cyclic and impact behaviour. Formulations for the cyclic stress-strain response and dynamic increase factors are also given while considering different rubber replacement ratios.

Experimental Program

Constituent materials

Ground granulated blast furnace slag (GGBS), complying with BS EN 15167-1 (2006), was used as the main aluminosilicate precursor, while low-calcium fly ash (FA), complying with BS EN 4501 (2012), was used as a supplementary precursor. The solid activator used was anhydrous sodium metasilicate (Na_2SiO_3) with a modulus of silicate (SiO_2/Na_2O) of 0.92. Sodium tetraborate decahydrate-borax ($Na_2B_4O_7.10H_2O$), with a mesh size of 2.36 mm, was used as a solid admixture. The fine natural aggregates (FNA) and coarse natural aggregates (CNA) employed were river sand and crushed gravel, respectively. Crumb rubber (CR) particles from discarded end-of-life tyres were used to replace a proportion of the total natural aggregates by volume. The physical properties of the constituent materials are listed in Table 1 while images of the constituent materials are given in Figure 1.

Material	**Specific gravity (-)**	**Median particle size, d_{50} (μm)**	**Size**	**Water absorption (%)**
GGBS	2.99	10.1	-	-
FA	2.33	22.6	-	-
FNA	2.67	-	0-5	1.3
CNA	2.69	-	5-10	3.0
CR	0.97	-	0-10 10-20	7.1 1.05

Table 1. Physical properties of constituent materials.

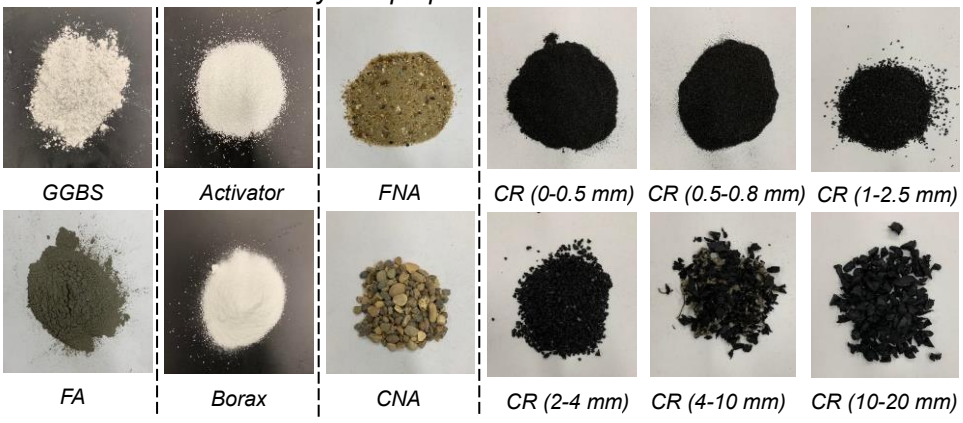

Figure 1. Constituent materials.

Mix designs and specimen preparation

Table 2 lists the mix designs investigated in this study. R00 is the reference non-rubberised mix optimized for high-strength and workability (Elzeadani et al., 2022b). R30 and R60 refer to mixes where 30 and 60% of the total natural aggregates are replaced with CR particles, giving a CR replacement ratio, ρ_{vr}, of 0.3 and 0.6, respectively. Concrete mixing was performed in a 40 L rotary mixing machine, and for each specific mix, the dry ingredients were initially mixed separately for 5 minutes followed by water addition and mixing for another 5-8 minutes. Slump tests were performed on the fresh concrete mixes in accordance with BS EN 12350-2 (2019), and R00, R30 and R60 mixes gave slump values in the range of 231-254, 203-245, and 153-210 mm, respectively.

The fresh concrete was then poured in concrete moulds and compacted using a vibrating table. The moulds were then covered with plastic sheets and kept in ambient laboratory conditions until demoulding two days after casting. Demoulded specimens were then stored in ambient conditions (temperature = 20±5 °C and relative humidity = 50±20%), until testing after 28 days of curing. In all cases, the ends of the cylindrical specimens were levelled to ensure smooth contact with the testing machines. For the non-rubberised specimens, this was done using a water grinding machine, while for the rubberised specimens, capping of the ends with high strength mortar was employed. Also, to avoid failure of the rubberised specimens at their ends due to potential rubber agglomeration during compaction, the ends were confined with stainless-steel jubilee rings.

Material	**R00**	**R30**	**R60**
GGBS	480	480	480
FA	120	120	120
Activator (Na_2SiO_3)	72	72	72
Admixture (Borax)	30	30	30
FNA	675	472.5	270
CNA	825	577.5	330
CR (0-0.5 mm)	0	8.1	16.3
CR (0.5-0.8 mm)	0	8.1	16.3
CR (1-1.25 mm)	0	24.4	48.8
CR (2-4 mm)	0	32.6	65.1
CR (4-10 mm)	0	16.3	32.6
CR (10-20 mm)	0	73.3	146.5
Water	180	180	180

Table 2. Concrete mix designs (kg/m³).

Cyclic tests

The cyclic tests were performed on a total of twenty-sevenØ 100×200 mm cylindrical specimens in an Instron Satec 3500 kN machine under displacement control conditions, as depicted in Figure 2(a). Displacement rates of 0.25, 25 and 250 mm/min were applied, giving rise to strain-rates of 2.08×10^{-5}, 2.08×10^{-3}, 2.08×10^{-2} s^{-1}, each, which correspond to quasi-static, moderate earthquake, and severe earthquake conditions, respectively. Three repetitive specimens were tested for each mix design and strain-rate.

Displacements in the pre-peak regime were determined from three transducers covering the middle 100 mm and spaced equally around the specimen. These transducers were mounted on steel rings connected to the specimens using three high-strength steel bolts. Displacements in the post-peak regime were captured using transducers placed on the loading platens of the testing machine. Strains were then determined from displacements using the relevant gauge length.

An incremental half-cyclic displacement was applied with three loading-unloading cycles at each displacement level as shown in Figure 2(b). Prior to reaching the crushing strength, the incremental displacement was set to 0.1 mm. This rate was increased gradually after reaching the peak crushing strength. In addition to the cyclic tests, twenty-seven Ø100×200 mm cylindrical specimens were tested under monotonic loading until failure at the various strain-rates considered to provide comparison with the cyclic tests.

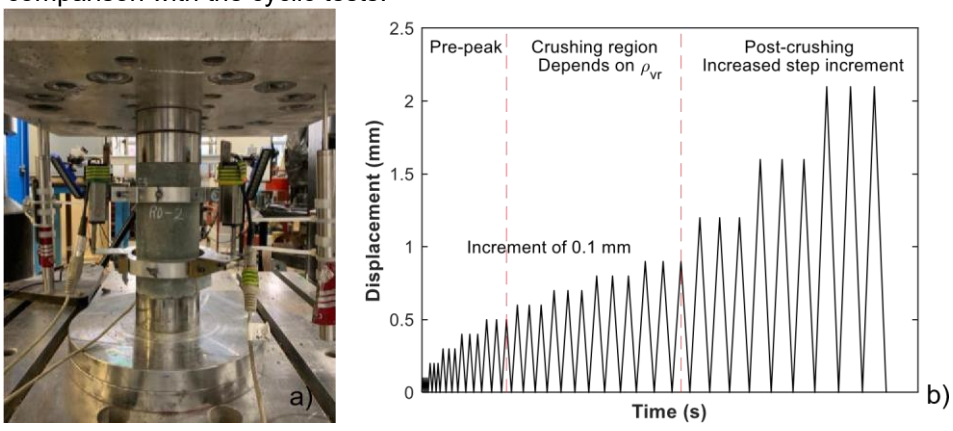

Figure 2. Cyclic tests: a) arrangement, b) loading sequence.

Impact tests

The impact tests were carried out in an Instron Dynatup 9250-HV loading rig with a drop tower, support table and a fixed base, as depicted in Figure 3(a). The drop tower had a drop-weight box fitted with an impactor head. The weight of the drop-weight box and impactor head was 6.5 kg, and an additional 20 kg can be added to the drop-weight box to give a varied range of impact energies. Additional impact energies can be obtained by driving the drop-weight box into springs available at the top of the drop tower. Due to limitations on the maximum impact force that can be applied by the Dynatup machine, the impact specimens tested for compression were Ø45×100 mm (a total of twenty-seven specimens) while those tested for splitting tension were Ø45×50 mm (twenty-seven specimens).

A load-cell capable of capturing up to two-million readings a second was placed at the bottom of the drop tower. Specimens tested in compression were placed on the load cell, and on top of that a 20 mm thickness steel plate and three pieces of carboarded were placed on the specimen as shown in Figure 3(b). Three impact speeds were considered, including 5, 10 and 15 m/s. For the latter two impact speeds, the 6.5 kg drop-weight box was used without any additional mass, whereas for the 5 m/s speed, the additional 20 kg mass was placed in the drop-weight box to generate enough energy to crush the specimens.

Displacements under impact loading were monitored using a digital image correlation (DIC) system made up of a single Phantom V611 high-speed camera with 50 mm f/1.8 lens. To ensure clear contrast in the images recorded, the surface of the specimens facing the camera was painted white and speckled with black dots. Part of the impactor head, steel plate above the specimen and the load cell – all in view of the camera – were also speckled to track their movements. For each specimen, a high-speed video of the test was recorded. This was later exported as a series of images to LaVision DaVis 10.2 software to post-process the images and obtain strain measurements.

A similar setup was employed for the splitting tensile impact specimens, however, the specimens this time were placed on their side inside a metal-plate holder, which was then placed in the loadcell at the bottom of the Dynatup machine (Figure 3(c)). The splitting tensile impact tests were carried out using the same impact speeds and impact weights as for the compressive cases and surface displacements were also monitored using DIC.

Figure 3. Impact tests: a) Impact loading rig, b) Impact compressive tests, c) Impact splitting tensile tests, d) quasi-static compressive tests, e) quasi-static splitting tensile tests.

The impact tests were accompanied by quasi-static tests on similar size specimens carried in an Instron Satec 600 kN machine under a displacement rate of 0.25 mm/min for the compressive cases and 0.1 mm/min for the splitting tensile cases, as shown in Figure 3(d) and Figure 3(e), respectively. Displacement readings were determined from a four-camera DIC system, with two cameras on each side of the specimen. Images for the quasi-static tests were taken at a rate of 1 Hz and then processed in LaVision 10.2 software.

Cyclic response

The average cyclic stress-strain (σ-ε) curves, together with their monotonic counterparts, are plotted in Figure 4. The naming format in Figure 4 follows Rxx-Sy-C/M, where Rxx refers to the mix design (i.e., R00, R30, R60), Sy refers the strain-rate, where S1, S2 and S3 refer to strainrates of 2.08×10^{-5}, 2.08×10^{-3}, 2.08×10^{-2} s^{-1}, respectively. C/M refer to the type of loading which is either cyclic or monotonic. As such, R60-S2-C refers to a Ø100×200 mm specimen with ρ_{vr} = 0.6 subjected to cyclic loading and a strain-rate of 2.08×10^{-3} s^{-1}.

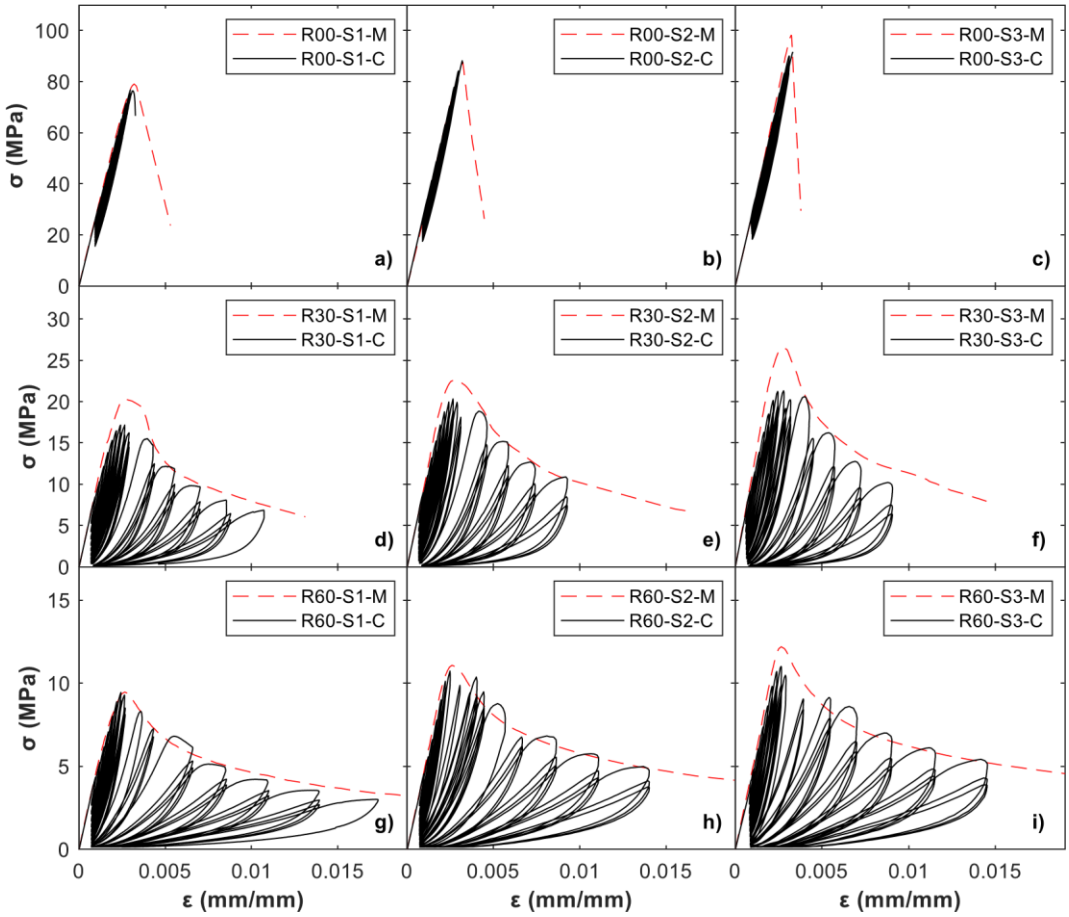

Figure 4. Rate-dependent cyclic stress-strain response: a) R00-S1, b) R00-S2, c) R00-S3, d) R30-S1, e) R30-S2, f) R30-S3, g) R60-S1, h) R60-S2, i) R60-S3.

The results show that the cyclic σ-ε curves fall within the monotonic response, and the latter can be taken as the envelope curves of the former. In addition, the rubberised specimens exhibited a clear post-peak cyclic degradation behaviour as opposed to the non-rubberised specimens which failed immediately after reaching the peak load. The compressive strength, f_c, and axial crushing strain, $\varepsilon_{cr,1}$, from the cyclic tests were generally lower than those recorded from the monotonic tests for the same strain-rate, $\dot{\varepsilon}$, and ρ_{vr}. This is likely due to slight damage accumulation during the loading and unloading cycles in the pre-peak regime. The elastic modulus, E_c, meanwhile, was marginally affected by the type of loading.

From the cyclic curves, an increase in ρ_{vr} from 0 to 0.3 and 0.6 caused a severe reduction in f_c by an average of about 77.1 and 87.8%, respectively, for all strain-rates considered. A similar effect was noted on E_c, where average reductions of nearly 66.4 and 83.0% were observed as ρ_{vr} increased from 0 to 0.3 and 0.6, respectively. These reductions are mainly due to the lower stiffness of CR particles in comparison to natural aggregates. The axial crushing strain, $\varepsilon_{cr,1}$, also experienced an average reduction of 16.1 and 21.6%, for all $\dot{\varepsilon}$ values considered, as ρ_{vr} increased from 0 to 0.3 and 0.6, respectively.

Specimens were also sensitive to $\dot{\varepsilon}$, generally showing an increase in f_c, E_c and $\varepsilon_{cr,1}$ in proportion to the rise in $\dot{\varepsilon}$. Furthermore, the results show that f_c was more sensitive to $\dot{\varepsilon}$, followed by E_c and then $\varepsilon_{cr,1}$. For instance, as $\dot{\varepsilon}$ increased from S1 to S2 and S3, f_c under cyclic loading increased by an average of 15.8 and 20.2%, respectively, for all rubber contents considered. For the same increase in $\dot{\varepsilon}$, the increase in E_c was 6.7 and 18.0%, respectively, while that for $\varepsilon_{cr,1}$ was 1.7 and 7.2%, respectively.

Impact response

Strain-rate readings for the impact specimens were determined by differentiating the strains obtained from the DIC system with respect to time. This gives the strain-rate time-history, and the selected strain-rate for a given impact scenario was taken as the peak strain-rate over the loading period. Looking at the compressive stress time-history results, an increase in the impact velocity caused an increase in the impact force and a reduction in the impact duration, regardless of the rubber content. However, an increase in the rubber content had the opposite effect of lower impact force and slightly greater impact duration.

Figure 5 depicts the dynamic stress-strain curves under impact for the specimens considered. The specimen reference employed in the figures follows Rxx-v, where Rxx refers to the mix design and v refers to the impact velocity. As such, R30-15 refers to specimens made of R30 mix and tested at an impact velocity of 15 m/s. The observed $\dot{\varepsilon}$ for each curve is shown in the legends of the figure.

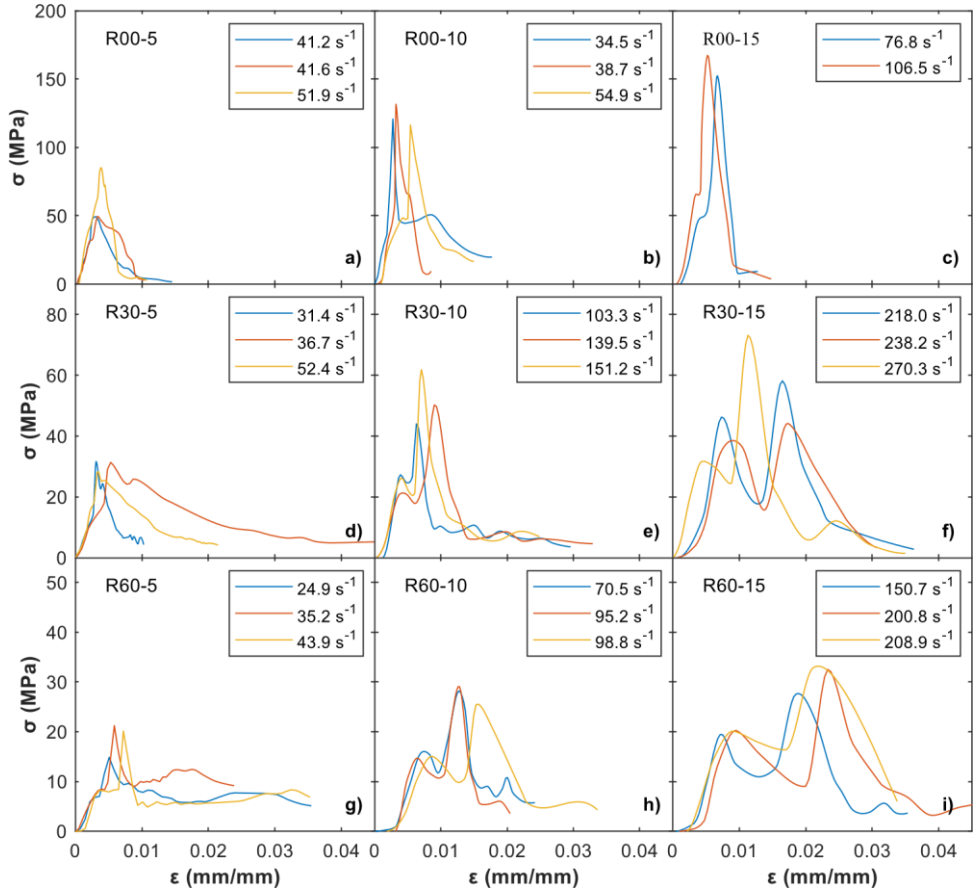

Figure 5. Dynamic stress-strain response under compressive impact loading: a) R00-5, b) R0010, c) R00-15, d) R30-5, e) R30-10, f) R30-15, g) R60-5, h) R60-10, i) R60-15.

Rubber addition seemed to influence the shape of the dynamic stress-strain curve. For instance, the non-rubberised specimens exhibited a single peak in the stress-strain response, while their rubberised counterparts experienced two major peaks. Such change due to rubber addition is likely due to the interception of stress waves by the softer rubber particles which supress crack development and act like springs, causing the stress-strain curve to rebound.

Analytical expressions

This section presents expressions characterising the cyclic and impact properties of OP-RuAAC. Expressions for predicting the monotonic mechanical properties and constitutive behaviour of similar mixes, developed by the authors, can be found elsewhere (Elzeadani et al., 2022b; Elzeadani et al., 2022c; Elzeadani et al., 2023).

Unloading modulus and plastic residual strain

The unloading modulus, E_{un}, in the cyclic stress-strain response is the stiffness of the unloading path as shown in Figure 6(a). Meanwhile, the plastic residual strain, ε_{pl}, is the axial strain at the end of a full unloading cycle as illustrated in Figure 6(a). Both E_{un} and ε_{pl} give indication of damage

accumulation in concrete with further unloading-reloading cycles. Eq. (1) presents an expression for E_{un} which takes into consideration $\varepsilon_{cr,1}$, ρ_{vr}, E_c and the unloading strain, ε_{un}. Eq. (2) gives an expression for ε_{pl}, which takes into account ε_{un} and $\varepsilon_{cr,1}$. Comparing such expressions with the experimental results, both Eq. (1) and (2) give reasonable predictions with average test-topredicted values (AVG) of 1.01 and 0.99, respectively, and coefficient of variations (COV) of 12.7 and 16.4%, respectively.

$$E_{unc} = 1.2 \times A^{-1.24} \rightarrow \varepsilon_{un} > \varepsilon_{cr,1} \quad (1)$$

$$A = (\varepsilon_{cr,1}^{\varepsilon_{un}} - 1) \times (-1.5\rho_{vr} + 2.5) + 1 \quad (2)$$

$$\varepsilon_{pl} = (7 \times \varepsilon_{cr,1}^{\varepsilon_{un}} - 2) \times 10^{-4} \rightarrow \varepsilon_{un} > \varepsilon_{cr,1} \quad (3)$$

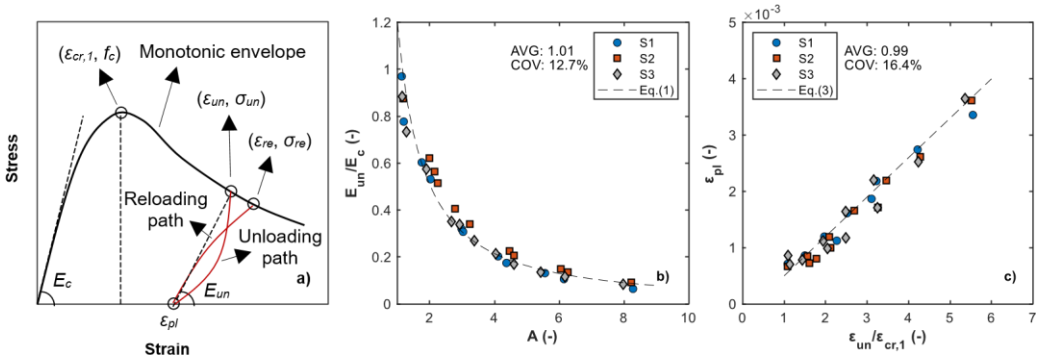

Figure 6. Characterisation of the cyclic response: a) concrete parameters under cyclic compression, b) unloading modulus, c) plastic residual strain.

Full unloading and reloading branches

The full unloading and reloading curves in the cyclic stress-strain curves can be represented by Eq. (4) and (5), respectively. The unloading branch is a function of the unloading stress (σ_{un}), ε_{un} and ε_{pl}, while the reloading branch is a function of σ_{un}, ε_{un}, ε_{pl}, and ρ_{vr}. Comparisons between the experimental and predicted unloading and reloading curves are given in Figure 7, showing generally good agreement between the results. In the predicted curves determined using Eq. (4) and (5), ε_{pl} was determined using Eq. (3) while ε_{un} was taken to coincide with the experimental values.

$$\sigma = \sigma_{un} \left(\frac{\varepsilon - \varepsilon_{pl}}{\varepsilon_{un} - \varepsilon_{pl}}\right)^3 \rightarrow \varepsilon_{pl} \leq \varepsilon \leq \varepsilon_{un} \; and \; 0 \leq \rho_{vr} \leq 0.6 \quad (4)$$

$$\sigma = 0.84 \times \sigma_{un} \left(\frac{\varepsilon - \varepsilon_{pl}}{\varepsilon_{un} - \varepsilon_{pl}}\right)^{(2-\frac{\rho_{vr}}{0.60})} \rightarrow \varepsilon_{pl} \leq \varepsilon \leq \varepsilon_{un} \; and \; 0 \leq \rho_{vr} \leq 0.6 \quad (5)$$

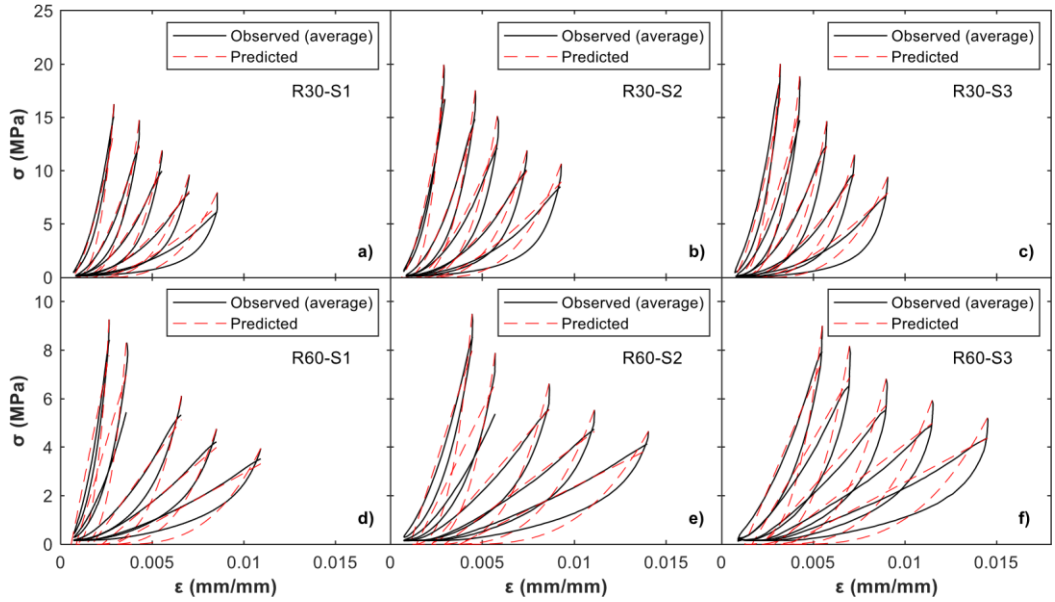

Figure 7. Unloading and reloading branches of the cyclic stress-strain response: a) R30-S1, b) R30-S2, c) R30-S3, d) R60-S1, e) R60-S2, f) R60-S3.

Dynamic increase factors

The dynamic increase factor (DIF) is the ratio of the dynamic strength to the quasi-static strength. From the results in this paper, DIF for the compressive strength, DIF_{fc}, crushing strain, $DIF_{\varepsilon cr,1}$, elastic modulus, DIF_{Ec}, and splitting tensile strength, DIF_{fsp}, are plotted against the logarithm of $\dot{\varepsilon}$, as given in Figure 8. Best-fit curves are also plotted alongside the results, which take the following form:

$$DIF = \begin{cases} A \log_{10} \dot{\varepsilon} + B, \dot{\varepsilon} < \dot{\varepsilon}_t \\ C \log_{10} \dot{\varepsilon} + D, \dot{\varepsilon} \geq \dot{\varepsilon}_t \end{cases} \quad (6)$$

where A, B, C and D are fitting coefficients determined from the test data, and $\dot{\varepsilon}_t$ is the transition strain-rate indicating a change in the slope of DIF best-fit curve. Such change in slope occurs as the DIF initially increases gradually with an increase in $\dot{\varepsilon}$ due to the effect of water viscosity in the concrete pores (i.e., Stefan effect). As $\dot{\varepsilon}$ reaches $\dot{\varepsilon}_t$, the DIF shoots up partly due to significant inertial and end-friction effects, and perhaps mainly due to the rapid formation of cracks under high $\dot{\varepsilon}$ that cross areas of high-resistance (i.e., aggregates) instead of forming in the weaker interfacial transition zones.

The fitting coefficients together with $\dot{\varepsilon}_t$ are given in Table 3. The results from Figure 8 and Table 3 mostly show a reduction in $\dot{\varepsilon}_t$ with higher ρ_{vr} for the various properties considered, indicating greater sensitivity of the rubberised concrete specimens to impact loading. Also, for a given $\dot{\varepsilon}$, the rubberised specimens tend to have a higher DIF in comparison to the non-rubberised specimens for the various mechanical properties investigated.

Property	Mix	A	B	Avg.[a]	COV[b]	C	D	Avg.[a]	COV[b]	$\dot{\varepsilon}_t$ (s^{-1})
DIF_{fc}	R00	0.0297	1.1725	1.00	0.05	3.8875	-4.0417	1.01	0.35	24.3
DIF_{fc}	R30	0.0984	1.4372	1.00	0.03	2.6959	-2.0013	1.00	0.15	20.9
DIF_{fc}	R60	0.0984	1.4448	1.00	0.01	2.6867	-1.0129	1.00	0.08	8.9
$DIF_{\varepsilon cr,1}$	R00	0.007	1.0321	1.00	0.00	2.2976	-2.6199	1.00	0.12	39.4
$DIF_{\varepsilon cr,1}$	R30	0.0069	1.0304	1.00	0.00	4.0667	-5.353	1.06	0.34	37.6
$DIF_{\varepsilon cr,1}$	R60	0.0088	1.0393	1.00	0.00	6.9311	-8.5002	1.03	0.19	24.8
DIF_{Ec}	R00	0.0161	1.0937	1.00	0.03	0.7954	0.1198	1.00	0.15	17.8
DIF_{Ec}	R30	0.0251	1.1621	1.00	0.06	0.5767	0.3658	1.01	0.12	27.5
DIF_{Ec}	R60	0.0302	1.1339	1.00	0.01	0.3759	0.650	1.01	0.10	25.1
DIF_{fsp}	R00	0.0169	1.0787	1.00	0.08	1.8475	-0.6513	1.02	0.20	8.9
DIF_{fsp}	R30	0.0451	1.2000	1.00	0.01	1.968	0.0795	1.02	0.12	3.9
DIF_{fsp}	R60	0.0898	1.3981	-	-	3.038	0.5106	1.00	0.08	2.0

Table 3. Eq. (6) fitting coefficients.

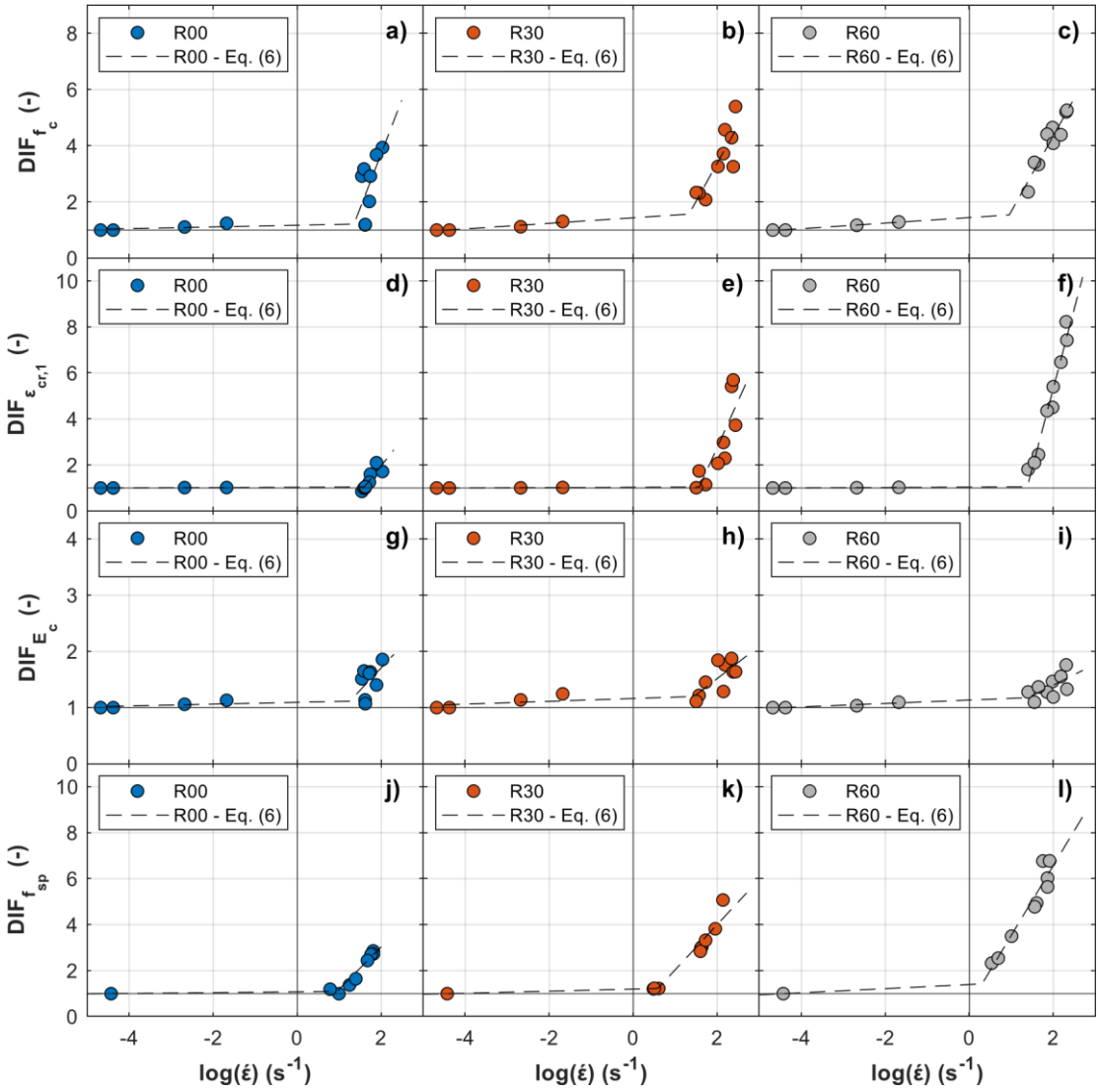

Figure 8. Dynamic increase factors: a) R00 DIF_{fc}, b) R30 DIF_{fc}, c) R60 DIF_{fc}, d) R00 $DIF_{\varepsilon cr,1}$, e) R30 $DIF_{\varepsilon cr,1}$, f) R60 $DIF_{\varepsilon cr,1}$, g) R00 DIF_{Ec}, h) R30 DIF_{Ec}, i) R60 DIF_{Ec}, j) R00 DIF_{fsp}, k) R30 DIF_{fsp}, l) R60 DIF_{fsp}.

Conclusions

This study examined the rate-dependent cyclic compressive properties of rubberised one-part alkali-activated concrete and their compressive and splitting tensile impact properties. Specimens of up to 60% volumetric replacement of the total natural aggregates were studied under a varied range of strain-rates, from 2.08×10^{-5} s^{-1} (quasi-static) to 270 s^{-1} (blast). The main findings of the study are as follows:

- Under both cyclic and impact conditions, an increase in rubber content caused a reduction in compressive strength, elastic modulus and splitting tensile strength. Moreover, an increase in rubber content caused an increase in the impact duration under compressive loading.
- The envelope of the cyclic stress-strain curves can be represented by their monotonic response.
- The shape of the compressive stress-strain response under impact loading was sensitive to the rubber content, showing two major peaks for the rubberised specimens in comparison to a single peak for the non-rubberised specimens.
- Rubberised specimens were more sensitive to the strain-rate, generally showing lower transition strain-rates and higher dynamic increase factors at a specific strain-rate.

- Formulations for the unloading modulus, plastic residual strain, full unloading and reloading branches of the cyclic stress-strain curves, and dynamic increase factors for the compressive strength, axial crushing strain, elastic modulus, and splitting tensile strength have been presented.

Acknowledgments

The first author acknowledges the funding provided by the President's PhD Scholarship at Imperial College London for his research studies. The assistance provided by Mr. Andy Pullen, a research fellow in the Department of Civil and Environmental Engineering at Imperial College London, in setting up the experimental programme for the impact tests is greatly appreciated. The support of the technical staff at the Structures Laboratory of Imperial College London, in particular Mr. Les Clark, Mr. Bob Hewitt, Mr. Paul Crudge, and Mr. Alfredo Olivo, with regards to the preparation and testing of specimens is highly appreciated.

References

Bompa DV, Elghazouli AY, Xu B, Stafford PJ and Ruiz-Teran AM (2017), Experimental assessment and constitutive modelling of rubberised concrete materials. *Construction and Building Materials*, 137: 246–260.

BS EN 450-1:2012, *Fly ash for concrete Part 1: Definition, specifications and conformity criteria*. 2012.

BS EN 12350 2:2019, *Testing fresh concrete Part 2: Slump test*. 2019.

BS EN 15167-1:2006, Ground granulated blast furnace slag for use in concrete, mortar and grout — Part 1: Definitions, specifications and conformity criteria. 2006.

Elzeadani M, Bompa DV and Elghazouli AY (2021), Preparation and properties of rubberised geopolymer concrete: A review. *Construction and Building Materials*, 313: 125504.

Elzeadani M, Bompa DV and Elghazouli AY (2022a), One part alkali activated materials: A state-of-the-art review. *Journal of Building Engineering*, 57: 104871.

Elzeadani M, Bompa DV and Elghazouli AY (2022b), Experimental assessment and constitutive modelling of rubberised one-part alkali-activated concrete. *Construction and Building Materials*, 353: 129161.

Elzeadani M, Bompa DV and Elghazouli AY (2022c), Mechanical properties and stress-strain response of rubberised one-part alkali-activated concrete, *in: 14th Fib PhD Symposium in Civil Engineering. Rome*, pp. 265–272.

Elzeadani M, Bompa DV and Elghazouli AY (2023), Monotonic and cyclic constitutive behaviour of rubberised one-part alkali-activated concrete. *Construction and Building Materials*, 368: 130414.

Pham TM, Chen W, Khan AM, Hao H, Elchalakani M and Tran TM (2020), Dynamic compressive properties of lightweight rubberized concrete. *Construction and Building Materials*, 238: 117705.

Provis JL (2018), Alkali-activated materials. *Cement and Concrete Research*, 114: 40–48.

Provis JL and Bernal SA (2014), Geopolymers and related alkali-activated materials. *Annual Review of Materials Research*, 44: 299–327.

Xu B, Bompa DV and Elghazouli AY (2020), Cyclic stress–strain rate-dependent response of rubberised concrete. *Construction and Building Materials*, 254: 1–14.